Ocean Engineering 333 (2025) 121491

Contents lists available at ScienceDirect

Ocean Engineering

journal homepage: www.elsevier.com/locate/oceaneng

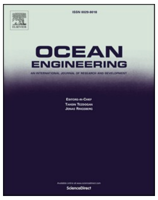

Research paper

Integrated IPC-TMDI control for mitigating fatigue in floating offshore wind turbines under misaligned wind-wave loading

Yida Pu [a], You Dong [a], Breiffni Fitzgerald [b,*]

[a] *Department of Civil and Environmental Engineering, The Hong Kong Polytechnic University, Hong Kong*
[b] *Department of Civil, Structural and Environmental Engineering, Trinity College Dublin, Dublin 2, Ireland*

ARTICLE INFO

Keywords:
Floating offshore wind turbine (FOWT)
Wind-wave misalignment
Fatigue damage assessment
Vibration control
Individual pitch control

ABSTRACT

As floating offshore wind turbines (FOWTs) increase in size, they become more efficient but also more susceptible to vibrations and fatigue, shortening their lifespan and reducing power generation. Existing control strategies often address these loads in isolation, limiting their effectiveness. This study proposes a cooperative control approach combining individual pitch control (IPC) with a side-to-side tuned mass damper inerter (TMDI) to mitigate tower fatigue under wind-wave misalignment. A multi-body dynamic model integrates a tower-top TMDI and a reduced-order IPC with an LQ controller to evaluate FOWT responses. Simulations of various wind-wave misalignment scenarios demonstrate that the cooperative approach significantly reduces fatigue damage equivalent loads (DELs) and stresses (DESs), extending tower fatigue life, particularly in high misalignment conditions.

1. Introduction

Wind energy holds significant potential for replacing fossil fuels due to its large-scale development feasibility and commercial prospects (G. W.E. Council, 2024a). To tap into the vast energy potential offshore, floating offshore wind farms (FOWFs) are emerging as a key focus, with projected growth in cumulative installed capacity (G.W.E. Council, 2024b). However, floating offshore wind turbines (FOWTs) face harsh wind and wave conditions that induce structural vibrations and fatigue. FOWTs experience large blade and tower vibrations and significantly fatigue damage equivalent loads (DELs) (Jonkman and Matha, 2009). Under significant wind-wave misalignment, insufficient damping in the lateral direction notably exacerbates both vibration and fatigue (Fischer et al., 2011; Dueñas-Osorio and Basu, 2008).

The blade pitch control system reduces aerodynamic loads for rated power production at wind speeds exceeding the rated threshold, lowering structural responses. The baseline controller (BC) uses a proportional–integral (PI) controller coupled with a collective pitch control (CPC) mode, which adjusts all three blades simultaneously. However, CPC cannot address asymmetric aerodynamic loads resulting from turbulence, wind shear, azimuth angle variations, and tower shadow (Jonkman et al., 2009).

The blade individual pitch control (IPC) mitigates asymmetric loads by independently adjusting each blade's pitch angle. Multi-blade coordinate (MBC) transformation maps loads into tilt and yaw directions, enabling individual pitch adjustments (Bir, 2010). Controllers like PI (Bossanyi, 2003) and linear quadratic Gaussian (LQG) (Wright, 2004) manage rotor speed and loads, while periodic control incorporates azimuth-related gains to capture higher-order load components beyond MBC (Namik and Stol, 2010). For floating offshore wind turbines (FOWTs), IPC also generates aerodynamic restoring moments, with platform and tower feedback reducing motion (Namik and Stol, 2010; Sarkar et al., 2021; Wakui et al., 2021; Fitzgerald and Sarkar, 2024).

Advanced pitch controllers integrate complex environmental factors, employing approaches like disturbance accommodating control (DAC) (Namik and Stol, 2014; Novaes Menezes et al., 2018; Lemmer et al., 2016), robust control (Yuan et al., 2020), adaptive control (Yuan and Tang, 2017; Zhang and Plestan, 2021a), model predictive control (MPC) (Odgaard et al., 2016), nonlinear MPC (NMPC) (Sarkar et al., 2020a), and sliding mode control (SMC) (Zhang and Plestan, 2021b). These model-based methods increasingly integrate data-driven techniques for enhanced performance (Zhang et al., 2022). Model-free data-driven control, which optimizes actions based on objectives or rewards without relying on system dynamics, presents an alternative approach (Xie et al., 2024; KhalafAnsar and Keighobadi, 2023).

Tuned mass dampers (TMDs) can be utilized alongside pitch control

---

* Corresponding author.
E-mail address: breiffni.fitzgerald@tcd.ie (B. Fitzgerald).

https://doi.org/10.1016/j.oceaneng.2025.121491
Received 9 December 2024; Received in revised form 23 April 2025; Accepted 6 May 2025

to suppress structure loads and vibrations of blades (Park and Lackner, 2021), towers (Lin et al., 2024), and floating platforms (Si et al., 2014) of wind turbines. TMDs are classified as passive, active (Fitzgerald et al., 2013), or semi-active (Sun, 2018), with various configurations such as tuned liquid dampers (TLDs), tuned liquid column dampers (TLCDs), rolling-ball dampers, eddy current TMDs (EC-TMDs), magneto-rheological elastomer TMDs (MRE-TMDs), shape memory alloy TMDs (SMA-TMDs), and pendulum pounding TMDs (PTMDs).

Passive TMDs are widely used due to their simplicity, low cost, and reliability, but space constraints in wind turbines limit their mass and stroke, reducing effectiveness (Fitzgerald and Basu, 2020). The TMDI was then created to remedy this. In 2002, Smith proposed the inerter (Smith, 2002), which generates inertial forces proportional to relative acceleration, effectively increasing mass without added weight. Commonly implemented with rack-and-gear or ball-screw mechanisms, inerters enhance TMD performance by amplifying mass effects and reducing damper stroke. TMDIs are particularly advantageous in wind turbines, offering improved vibration control in limited space (Fitzgerald et al., 2023; Sarkar and Fitzgerald, 2020, 2022).

Active control strategies, such as generator torque control (Zhang et al., 2014; Wang et al., 2024), trailing edge flaps (Chen et al., 2017), and active mooring force control (Wu and Li, 2020), play a vital role in mitigating wind turbine loads.

Integrated approaches, like multi-mode TMDs (MTMDs) (Dinh and Basu, 2015; Zuo et al., 2017; Li et al., 2022; Chen et al., 2021) and multi-directional vibration control (Jahangiri and Sun, 2020), can further enhance control effectiveness by combining multiple controllers. For instance, combining torque and pitch control reduces wave-induced loads in offshore turbines (Chen et al., 2024). In the author's previous work about IPC (Sarkar et al., 2021), IPC was found to be able to effectively suppress the tower fore-aft response, but it performs similarly as the baseline controller in wind-wave misalignment cases. In other work about TMDI (Sarkar and Fitzgerald, 2020, 2022) by the author, TMDI was found less efficient in the fore-aft direction due to a large amount of aerodynamic damping. Therefore, the integrated IPC-TMDI control system integrated the advantages of single IPC and TMDI. Meanwhile, there is no mutual influence due to weak coupling in two different motion directions, which makes the controller design simple. While Tang et al. (2024) integrated fore-aft TMDI and IPC for onshore turbines, side-to-side TMDI is more effective for FOWTs under misaligned wind-wave loads due to limited damping in this direction.

This study introduces a cooperative control strategy for FOWTs, integrating a side-to-side TMDI to mitigate tower vibrations and IPC to stabilize fore-aft motion and power output. A nonlinear FOWT model evaluates four control strategies under steady wind and wave-free conditions, comparing their effectiveness in reducing tower damage equivalent loads (DELs), design equivalent stresses (DESs), and extending tower fatigue life under varying wind-wave misalignments. Results highlight the benefits of this integrated approach.

2. Cooperative control strategy for FOWT

2.1. Modeling of FOWT

A nonlinear aeroelastic model utilizing multi-body dynamic (MBD) method is employed to obtain the structural responses of the FOWT and further analyze structural fatigue damage. The model is constructed utilizing Kane's approach (Kane and Levinson, 1985) by Sarkar et al. (Sarkar and Fitzgerald, 2021), and it includes 22 degrees of freedom (DOFs)to present the tower, the floating platform, the nacelle, the blades, the drive-train, and the generator, as detailed in Table. A1 in the appendix. The TurbSim program (Jonkman, 2009) is utilized to create the turbulent wind fields, while the Pierson–Moskowitz spectrum (Pierson and Moskowitz, 1964) is employed to represent stochastic waves. The hydrodynamic loads are then estimated using Morison's method and the aerodynamic loads are predicted utilizing the blade element momentum (BEM) approach. MoorDyn (Hall, 2015) is utilized to represent the force of mooring cables. The fully coupled computing framework is shown in Fig. 2. More details about modeling FOWT can be found in (Sarkar and Fitzgerald, 2021). To regulate the structural response, the nonlinear FOWT model is integrated with various controllers, created and executed in MATLAB (MathWorks Inc, 2023). More details about the multi-body FOWT model can be seen (Fitzgerald et al., 2023; Sarkar and Fitzgerald, 2020, 2021; Sarkar et al., 2020b). OpenFAST (Jonkman and Buhl, 2005), a fully coupled nonlinear simulation tool, has been used to benchmark and validate the nonlinear FOWT model, excluding the coupled damper (Sarkar and Fitzgerald, 2021).

The NREL 5 MW OC3 spar-buoy type FOWT is taken as the reference since it was widely used in literature and international research projects. Key parameters for the selected FOWT structure are listed in Table 1. More details about the structural and aerodynamic properties of the tower and the blades are defined in (Jonkman et al., 2009).

2.2. IPC with LQ controller and integral controller

The IPC uses an integrated controller in conjunction with a LQ controller to calculate each blade pitch angle individually. A schematic of IPC is shown in Fig. 3. The collective pitch command, θ, and the individual pitch command, Θ_I, combine to form the total blade pitch command, Θ:

$$\Theta = \theta + \Theta_I \tag{1}$$

The integral controller generates the collective pitch command, ensuring that the rotor speed can converge to the nominal speed at wind speeds exceeding the rated threshold. The individual pitch angles are produced by the LQ controller, for regulating along-wind dynamic response. As shown in Fig. 3, the control commands are saturated before feedback occurs to give realistic control actions. Besides, the generator speed undergoes the designed low-pass filter in order to eliminate any high-frequency signal. The integral controller has been obtained from (Jonkman et al., 2009) and (Jonkman, 2010) based on the motion equation of the shaft angular rotation DOF, where the integral coefficient K_I is selected to create a positively damped controller by adjusting the controller frequency. A reduced-order 6-DOF model is constructed to design the LQ controller, and the selected DOFs are as follows:

Table 1
Key parameters for the FOWT structure.

Component	Parameter	Value	Parameter	Value
Rotor & Blades	Rotor Diameter	126 m	Rated Rotor Speed	12.1 rpm
	Blade Length	61.5 m	Cut-in Wind Speed	3 m/s
	Number of Blades	3	Cut-out Wind Speed	25 m/s
	Hub Height	90 m	Blade Mass (each)	17,740 kg
	Rated Power	5 MW	Airfoil Type	DU/NACA
Tower	Height	87.6 m	Wall Thickness	0.027–0.05 m
	Top Diameter	3.87 m	Mass	347,460 kg
	Base Diameter	6 m	Material	Steel
Floating Platform	Type	Spar-buoy	Ballast Mass	1,200,000 kg
	Length	120 m	Total Structure Mass	7,466,330 kg
	Outer Diameter	6.5 m	Gravity Center	29 m
Mooring System	Type	Catenary	Line Length	902.2 m
	Number of lines	3	Line Diameter	0.09 m
	Fairlead Radius	5.2 m	Pretension	200 kN
	Anchor Radius	853.87 m	Line Material	Steel Chain

$$\mathbf{x} = \{q_P \; q_{TFA1} \; q_{B1F1} \; q_{B2F1} \; q_{B3F1} \; q_\varepsilon\} \tag{2}$$

q_ε is generator speed error DOF, and other DOFs can be found in table. A1. Kane's approach is used again to construct the reduced-order model, and then the nonlinear model is linearized as state space expression. The rotor is believed to spin steadily so that the rotor and generator speeds keep constant, and the errors become zero. The final motion equation is then fromed by combining the generator speed error DOF with the 5-DOF system. The motion equation for individual generator speed error DOF is:

$$I_{DT}\ddot{q}_\varepsilon + \left(-\frac{P_0}{\Omega_0^2}\right)\dot{q}_\varepsilon + \frac{1}{\Omega_0}\left(-\frac{\partial P_0}{\partial \theta}\right)N_{Gear}K_I q_\varepsilon = 0 \tag{3}$$

$$\dot{q}_\varepsilon = \delta\Omega = \Omega_0 - q_{GeAz} \tag{4}$$

$$q_\varepsilon = \int_0^t \dot{q}_\varepsilon dt = \int_0^t (\Omega_0 - q_{GeAz})dt \tag{5}$$

$$\ddot{q}_\varepsilon = \delta\dot{\Omega} = \ddot{q}_{GeAz} \tag{6}$$

where Ω_0 represents the rated rotor speed of the FOWT, I_{DT} represents inertia from the drivetrain, P_0 represents the rated mechanical power, θ represents the blade pitch angle, N_{Gear} represents the gear box ratio, and ω_ε represents the frequency of this DOF. Therefore, mass, stiffness, and damping terms for the generator speed error are:

$$m_\varepsilon = I_{DT} \tag{7}$$

$$k_\varepsilon = \frac{1}{\Omega_0}\left(-\frac{\partial P_0}{\partial \theta}\right)N_{Gear}K_I = \omega_\varepsilon^2 I_{DT} \tag{8}$$

$$c_\varepsilon = \left(-\frac{P_0}{\Omega_0^2}\right) \tag{9}$$

After adding these terms to the 5-DOF system, the final 6-DOF system can be obtained. More details about the mass, stiffness, and damping matrices of final linearized system can be found in the author's previous work (Sarkar et al., 2021). The resulting motion equation for the linearized 6-DOF system can be expressed as follows:

$$\mathbf{M}\ddot{\mathbf{q}} + \mathbf{C}\dot{\mathbf{q}} + \mathbf{K}\mathbf{q} = \mathbf{F}_{Areo}(v, \Theta) + \mathbf{F}_{Hydro}(H_s, T_p) \tag{10}$$

In (10), the wind speed v and blade pitch angles Θ determine the aerodynamic load $\mathbf{F}_{Areo}$, and the wave parameters, H_s and T_p, determine the hydrodynamic load $\mathbf{F}_{Hydro}$. Afterwards, the motion equation can be further expressed in state space as:

$$\dot{\mathbf{x}} = \mathbf{A}\mathbf{x} + \mathbf{B}(\Theta)\Theta + \mathbf{G}(v, \Theta, H_s, T_p) \tag{11}$$

where $\mathbf{x} = [\mathbf{q}; \dot{\mathbf{q}}] \in \mathscr{R}^{12\times1}$ represents the state vector, and $\mathbf{B}(\Theta)$ represents the control input matrix determined by the blade pitch command $\Theta \in \mathscr{R}^{3\times1}$. But in this study, the control input matrix $\mathbf{B}(\theta)$ is assumed to be equivalent to $\mathbf{B}(\Theta)$ for a simpler controller design, so the control input matrix can be derived as follows:

$$\mathbf{B}(\theta) = \frac{\partial \mathbf{F}_{Aero}}{\partial \theta}|_{v_0,\theta_0} \tag{12}$$

More specifically, it is the numerical central difference method that is utilized to obtain the control input matrix at the operating point. The external disturbance factors in Eq. (10) and Eq. (11) are ignored, and the LQ controller remains steady-state under all load conditions. The steady-state LQ controller cannot depict all the dynamic features of a finite-time system at the operating point, but this method is commonly used (Namik and Stol, 2010, 2014). It facilitates controller design because of no need for working out an additional set of differential equations. The LQ controller is designed to minimize the cost function, which is shown as:

$$J = \int_0^\infty \left(\mathbf{x}^T\mathbf{Q}\mathbf{x} + \Theta_l^T\mathbf{R}\Theta_l\right)dt \tag{13}$$

in which $\mathbf{Q}$ and $\mathbf{R}$ stand for the state and input weight matrices, respectively, that punish the states of the control system and the control input vector, respectively. The optimal control can be found solving the Ricatti equation:

$$\mathbf{PA} + \mathbf{A}^T\mathbf{P} - \mathbf{PB}(\theta)\mathbf{R}^{-1}\mathbf{B}^T\mathbf{P} + \mathbf{Q} = \mathbf{0} \tag{14}$$

$$\Theta_l = -\mathbf{R}^{-1}\mathbf{B}(\theta)\mathbf{P}\mathbf{x}(t) = -\mathbf{K}(\theta)\mathbf{x}(t) \tag{15}$$

As a result, the LQ controller gain matrix can be tuned by modifying the state and input weight matrices. More details about the tuning process are shown in Section 3.2.1.

2.3. Side-to side TMDI

The passive side-to-side TMDI is investigated in this portion. As seen in Fig. 4 (a), the side-to-side TMDI is mounted at the tower top to mitigate side-to-side vibrations. Fig. 4 (c) shows that the inerter is connected to the mass unit in parallel with the spring and damper units. The inerter transforms the linear motion of the physical mass into the rotating motion of ball screw or flywheel, while also producing a mass enhancement effect. This effect enables the TMDI to use the lighter physical mass yet provides improved vibration control.

The TMDI position does not affect other parts of the FOWT, making the installation of the TMDI simple. Hence, the position vectors and velocity vectors for other parts remain unchanged. The DOF number of the nonlinear FOWT model rises to 23 with the addition of the TMDI, and this model needs to include the position vector of TMDI as follows:

$$r^{OD} = \begin{cases} q_D\widehat{\mathbf{b}}_3 \\ q_D\widehat{\mathbf{b}}_1 \end{cases} \tag{16}$$

in which r^{OD} represents the position vector of the TMDI from the origin of the tower top coordinate to its mass center; q_D represents its displacement; $\widehat{\mathbf{b}}_1$ and $\widehat{\mathbf{b}}_3$ represent the fore-aft and side-to-side directions in this coordinate system, respectively, which can be found in Fig. 1. The inerter, damper, and spring units of the TMDI provide the generalized active forces while the mass unit contributes to the generalized inertia forces.

2.3.1. Optimal tuning of TMDI

The TMDI's ideal tuning parameters are determined by applying white noise to a simplified 2-DOF model (Marian and Giaralis, 2014),

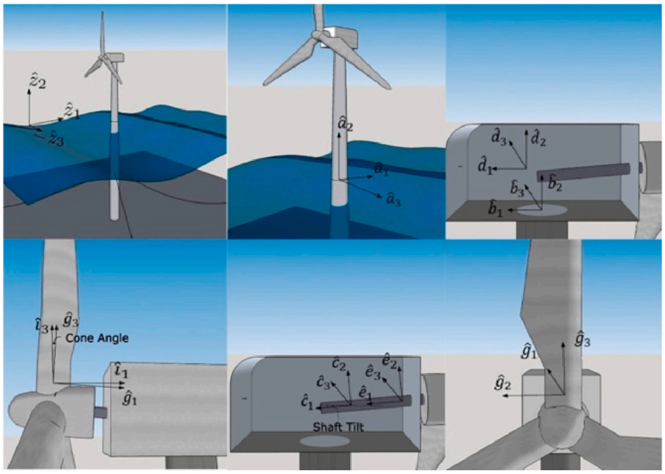

Fig. 1. Multiple coordinate systems of the spar-type FOWT.

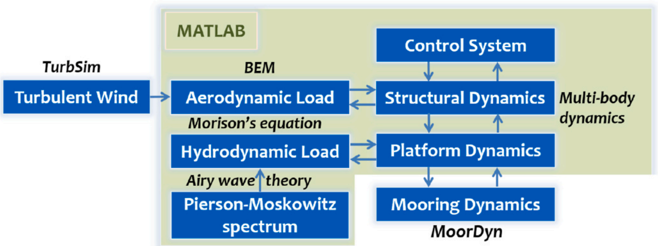

Fig. 2. Fully coupled computing framework.

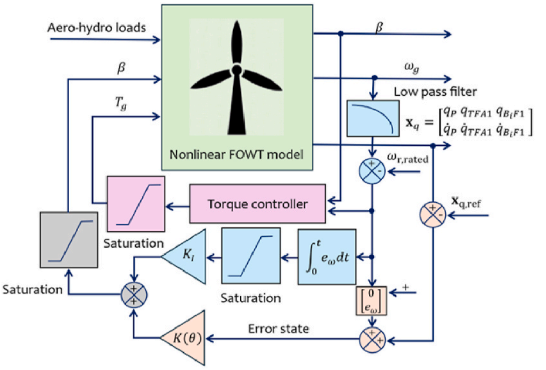

Fig. 3. Schematic of IPC.

which is shown in Fig. 4 (b). More details about the simplified 2-DOF model can be found in the author's previous work (Sarkar and Fitzgerald, 2020, 2021). The normalized motion equation of the reduced model is as follows:

$$\begin{bmatrix} 1+\mu+\beta(1-\phi)^2 & \mu+\beta(1-\phi) \\ \mu+\beta(1-\phi) & \mu+\beta \end{bmatrix}\begin{pmatrix} \ddot{q}_t \\ \ddot{q}_d \end{pmatrix} + \begin{bmatrix} 0 & 0 \\ 0 & 2\mu\omega_t\zeta_d\omega_r \end{bmatrix}\begin{pmatrix} \dot{q}_t \\ \dot{q}_d \end{pmatrix}$$

$$+\begin{bmatrix} \omega_t^2 & 0 \\ 0 & \mu\omega_t^2\omega_r^2 \end{bmatrix}\begin{pmatrix} q_t \\ q_d \end{pmatrix} = \begin{pmatrix} \dfrac{F}{m_0} \\ 0 \end{pmatrix} \tag{17}$$

where q_t and q_d are the tower and the TMDI DOFs, respectively. μ is the mass ratio and β is the inerter ratio, and they are defined as:

$$\mu = \frac{m_d}{m_0} \tag{18}$$

$$\beta = \frac{b}{m_0} \tag{19}$$

where m_d is the physical mass and b is the inertial mass, both with the unit of mass. The natural frequencies of the tower and TMDI are denoted by ω_t and ω_d, respectively. The tuning ratio and damping ratio of the TMDI are defined as

$$\omega_r = \frac{\omega_d}{\omega_t} \tag{20}$$

$$\zeta_d = \frac{c_d}{2m_d\omega_d} \tag{21}$$

where c_d represents the damping coefficient of the damping unit. ϕ denotes the tower mode factor at the height H_I, as follows:

$$\phi = \phi_t(H_I) \tag{22}$$

in which ϕ_t denotes the normalized primary mode shape of the tower, so $0 \le \phi \le 1$. Once the mode factor ϕ and white noise F are determined, the optimal tuning ratio can be derived according to (Sarkar and Fitzgerald, 2020) as follows:

$$\omega_r = \sqrt{\frac{-B+\sqrt{B^2-AC}}{2A}} \tag{23}$$

where

$$A = 3\mu^2\left(\mu^2+2\mu\phi^2\beta-4\mu\phi\beta+2\mu\beta+2\mu+\phi^4\beta^2-4\phi^3\beta^2+6\,\phi^2\beta^2 \right.$$
$$\left. +2\phi^2\beta-4\phi\beta^2-4\phi\beta+\beta^2+2\beta+1\right)$$

$$B = \mu\left(4\mu^2\zeta_d^2-\mu^2+4\mu\phi^2\zeta_d^2\beta-2\mu\phi^2\beta-8\mu\phi\zeta_d^2\beta+2\mu\phi\beta \right.$$
$$\left. +4\mu\zeta_d^2\beta+4\mu\zeta_d^2-2\mu\beta-2\mu-\phi^2\beta^2+\phi\beta^2-\beta^2-2\beta\right)$$

$$C = -\left(\mu^2+2\mu\beta+\beta^2\right)$$

and the optimal damping ratio

$$\zeta_d = \frac{1}{2\mu\omega_r}\sqrt{\frac{D}{E}} \tag{24}$$

where

$$D = \mu^4\omega^4+2\mu^3\phi^2\beta\omega_r^4-4\mu^3\phi\beta\omega_r^4+2\mu^3\beta\omega_r^4+2\mu^3\omega_r^4-\mu^3\omega_r^2+\mu^2\phi^4\beta^2\omega_r^4$$
$$-4\mu^2\phi^3\beta^2\omega_r^4+6\mu^2\phi^2\beta^2\omega_r^4+2\mu^2\phi^2\beta\omega_r^4-2\mu^2\phi^2\beta\omega_r^2-4\mu^2\phi\beta^2\omega_r^4$$
$$-4\mu^2\phi\beta\omega_r^4+2\mu^2\phi\beta\omega_r^2+\mu^2\beta^2\omega_r^4+2\mu^2\beta\omega_r^4-2\mu^2\beta\omega_r^2+\mu^2\omega_r^4-2\mu^2\omega_r^2$$
$$+\mu^2-\mu\phi^2\beta^2\omega_r^2+2\mu\phi\beta^2\omega_r^2-\mu\beta^2\omega_r^2-2\mu\beta\omega_r^2+2\mu\beta+\beta^2$$

$$E = \mu+\phi^2\beta-2\phi\beta+\beta+1$$

Eqs. (23) and (24) become the ideal tuning parameters of conventional TMDs when the inertial mass vanishes and the fundamental structure is subjected to the same white noise. Indefinitely increasing the physical and inertial mass of the TMDI is not an optimal strategy for enhancing its performance. The excessive physical mass at the tower top can lead to platform instability and excessive vibrations. Also, research has shown that the vibration control efficacy of TMDIs reaches a

(a) Side-to-side TMDI placed inside the nacelle

(b) Reduced model with a TMDI and the tower

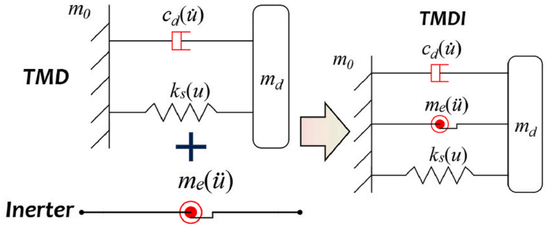

(c) TMDI and TMD

Fig. 4. Schematic of Tmdi.

saturation point when the inerter ratio β exceeds 0.4 (Sarkar and Fitzgerald, 2020). Hence, in this study, the mass ratio μ is taken as 0.01 and the inerter ratio β is taken as 0.4. Additionally, it is assumed that the inerter is hooked at 0.7 times tower height, $H_I = 0.7H_t = 54.32$ m. As a result, the optimal tuning ratio ω_r and optimal damping ratio are further obtained by the iterative procedure, $\omega_r = 5.8896$, and $\zeta_d = 1.0521$.

2.4. *Cooperative control strategy under wind-wave misalignment*

According to section 2.2, the IPC is designed to regulate power production and along-wind dynamic response, since the generator speed error DOF and several along-wind DOFs (q_P, q_{TFA1}, and q_{B_iF1}) are chosen. Apart from the functions that reduce the along-wind asymmetrical loads and regulate power generation performance, IPC can actually function to suppress the side-to-side motion of WTs through sideway force on the hub produced by disequilibrium edgewise shear forces at the blade roots (Fischer et al., 2011). Nevertheless, this requires that the IPC include sideway states or feedback, which conflicts with the along-wind states-based IPC, not considered in this study.

TMDIs can be mounted at the tower top, either fore-aft or side-to-side, to reduce tower vibrations. However, due to greater aerodynamic damping in the fore-aft direction, side-to-side TMDIs are generally more effective (Sarkar and Fitzgerald, 2020, 2022). For this study, as seen in Fig. 4(a), a side-to-side TMDI is placed at the tower top to suppress target vibrations. This is crucial under wind-wave misaligned conditions, where side-to-side vibrations become as significant as fore-aft vibrations for fatigue analysis (International Electrotechnical Commission, 2020). The cooperative control strategy combines the strengths of IPC and TMDI, compensating for each other's limitations without interference, as weak coupling allows straightforward design for each controller (Fig. 5).

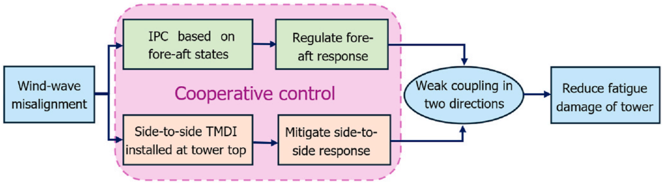

Fig. 5. Schematic diagram of the integrated IPC-TMDI control.

3. Performance evaluation of the cooperative control strategy

3.1. *Under steady wind and wave-free*

The proposed cooperative control strategy is first evaluated against BC without TMDI, BC with TMDI, and IPC without TMDI under the steady wind and wave-free scenario to study the FOWT's transient response. MATLAB (MathWorks Inc, 2023) is used as the simulation platform, and the fourth-order Runga-Kutta approach is applied for temporal integration. It is assumed that the FOWT is exposed to a steady wind field with the hub height reference wind speed of 18 m/s and is floating on still water. The state weight matrix is taken as $\mathbf{Q} = 0.001\times \mathbf{I}_{11\times 11}$ to reduce the pitch actuation while the control weight matrix is taken as a third-order identity matrix, $\mathbf{R} = \mathbf{I}_{3\times 3}$. The final low-authority IPC is obtained by further modifying the state weight matrix **Q,** assigning a weight of 1 to the tower fore-aft, platform pitch, and generator azimuth states. The optimal tuning parameters for TMDI are assigned as those in section 2.3.

Fig. 6 (a)–(f) shows the structural dynamic response of the FOWT, including blade out-of-plane and in-plane deflection, tower top fore-aft and side-to-side displacement, as well as platform pitch. Fig. 6. (g) and Fig. 6. (i) show the rotor speed and power generation, which are expected to follow reference values, respectively. Meanwhile, Fig. 6. (h) illustrates the pitch angle of blade 1. These results elucidate the distinct functions of TMDI and IPC: TMDI primarily reduce tower side-to-side response with minimal impact on other responses, whereas IPC enhances the tracking of the rated generator power and the rated rotor speed, while also mitigating blade response and tower fore-aft response. Although the tower side-to-side response is much lower than the tower fore-aft response under this steady wind and wave-free condition, the former would be significant under wind-wave misalignment, where the TMDI can play an important role. Furthermore, as seen in Fig. 6 (a), the rise in pitch actuation is necessary to suppress structural response, although the pitch actuation remains within saturation limits.

3.2. *Under wind-wave misalignment*

In this part, frequency domain analysis is used to illustrate the dynamic response under wind-wave misalignment loads. Additionally, the variations in structural response and controller performance due to increasing misalignment degrees are investigated through fatigue analysis. The mean wind speed at the hub height is 18 m/s, and the Kaimal turbulence model is considered, with the turbulence intensity of the wind field classified as Class B, according to the NTM in IEC 61400–1 (International Electrotechnical Commission, 2019). The wave period is 7.30 s with wave heights of 2.41 m. Before carrying out the simulation, the next section introduces the optimal tuning of IPC for regulating power generation and tower fore-aft dynamic response.

3.2.1. *IPC optimal tuning*

The integral gain has been determined according to (Jonkman, 2010), and the construction of the LQ controller requires the determination of the input and state weight matrices. The control weight matrix is still chosen as $\mathbf{R} = \mathbf{I}_{3\times 3}$. To reach an optimal balance between power regulation and tower fore-aft dynamic response, a cost function is employed to determine optimal tuning parameters within the state weight matrix **Q**, as follows:

$$J = \Psi_P + \Psi_{DEL} \tag{25}$$

Ψ_P represents the control performance in reducing power variability and Ψ_{DEL} depicts the control performance in reducing damage equivalent load (Ψ_{DEL}) for the tower base fore-aft bending moment. They are defined as follows:

$$\Psi_P = \frac{\sigma_{IPC}}{\sigma_{BC}} \tag{26}$$

$$\Psi_{DEL} = \frac{\Delta_{IPC}}{\Delta_{BC}} \tag{27}$$

where σ denotes the power error root mean square (RMS) and Δ represents the fatigue DEL of the tower base fore-aft bending moment. The state weight matrix **Q** is defined as:

$$\mathbf{Q} = \begin{bmatrix} \mathbf{Q}_l(1-\rho) & \cdots \\ \cdots & \rho \end{bmatrix} \tag{28}$$

where, $\mathbf{Q}_l = 0.001 \times \mathbf{I}_{11\times 11}$, and it is further adjusted by assigning a weight of 1 to the tower and platform states. The cost function depicted in Fig. 7 is obtained by sweeping the tuning parameter ρ. The ideal tuning parameter ρ is found by comparing the cost function values under four distinct wind-wave loading scenarios.

Based on a visual analysis of the cost function values presented in Fig. 7, the tuning parameter ρ is best adjusted to 0.6 to minimizes the cost function and reaches the best possible balance between the two conflicting goals.

3.2.2. *Control performance evaluation*

Fig. 8 demonstrates that the TMDI exerts minimal influence on the blade response, so the cooperative control strategy acts like the single

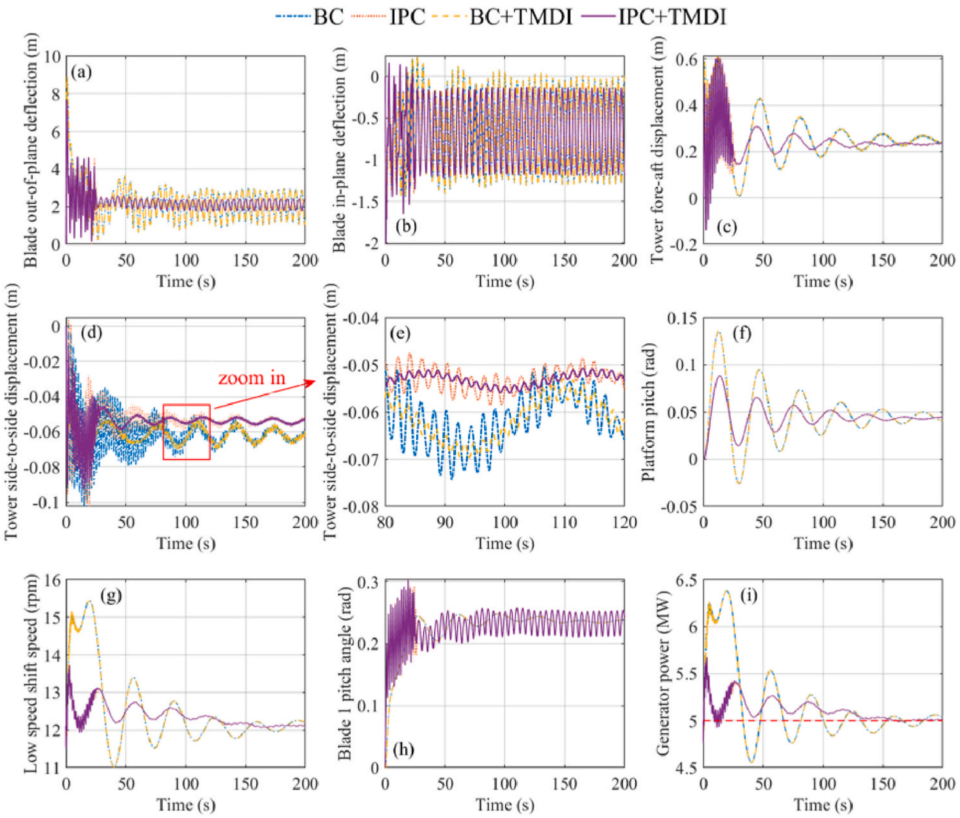

Fig. 6. Dynamic response of FOWT under steady wind and wave-free. (a) Blade out of plane. (b) Blade in-plane. (c) Tower fore–aft. (d) Tower side-to-side. (e) Zoom in tower side-to-side. (f) Platform pitch. (g) Rotor speed. (h) Blade 1 pitch. (i) Generator power.

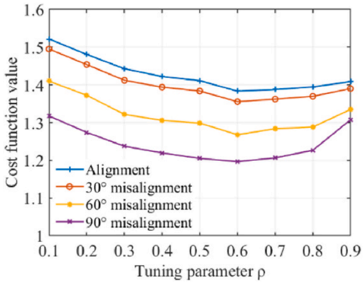

Fig. 7. Effect of the tuning parameter ρ on cost function value.

IPC to reduce the blade response by regulating the IP frequency component.

As shown in Fig. 9 (a) and (b), IPC is capable of mitigating the tower fore-aft response mostly by regulating the platform pitch, whereas TMDI can increase the tower damping to mitigate the tower side-to-side response. IPC can efficiently adjust the fore-aft aerodynamic input, which is more effective than increasing the structural damping. However, in the lateral direction, the TMDI demonstrates effective performance due to the relatively low aerodynamic damping.

To assess the different control approaches, fatigue damage is considered as a main objective for comparison. The tower DELs are calculated using the classical rain flow counting technique (Downing and Socie, 1982), and single slope S-N curve from MLife (Hayman, 2012) is adopted:

$$DEL^{ST} = \left(\frac{\sum_i (n_i L_i)^m}{f_{eq} T_e}\right)^{1/m} \tag{29}$$

where ST denotes that the fatigue analysis is carried out according to short-term time series; n_i represents the cycle count; L_i represents the load range; f_{eq} represents the damage-equivalent load frequency; T_e represents the elapsed time of time-series; m represents the Whöler exponent. For blades with composite structures, the Whöler exponent m ranges from 3 to 4, while for steel towers, this figure falls between 9 and 13 (Avendaño-Valencia et al., 2021). In this study, the Whöler exponent m is taken as 4 and 10 for blades and tower, respectively.

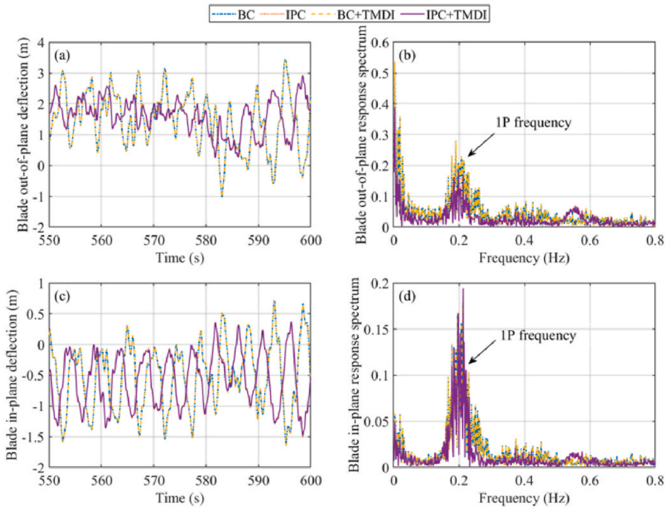

Fig. 8. Dynamic response of FOWT blade subjected to 90° wind-wave misalignment loading. (a) Blade out-of-plane deflection. (b) Blade out-of-plane response spectrum. (c) Blade in-plane deflection. (d) Blade in-plane response spectrum.

Fig. 10 displays the schematic diagram of the wind-wave

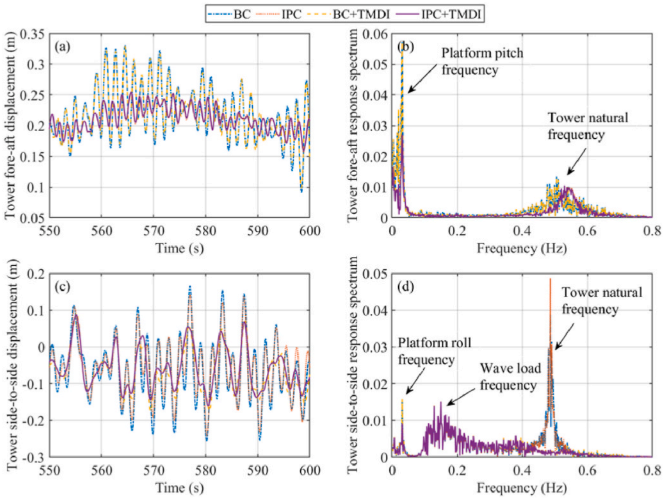

Fig. 9. Dynamic response of FOWT tower subjected to 90° wind-wave misalignment loading. (a) Tower fore-aft displacement. (b) Tower fore-aft response spectrum. (c) Tower side-to-side placement. (d) Tower side-to-side response spectrum.

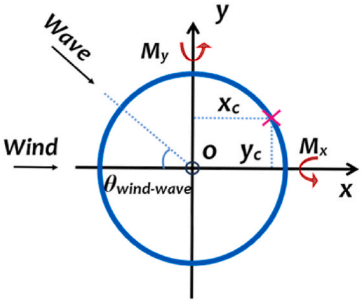

Fig. 10. Schematic of wind-wave misalignment and tower cross-section.

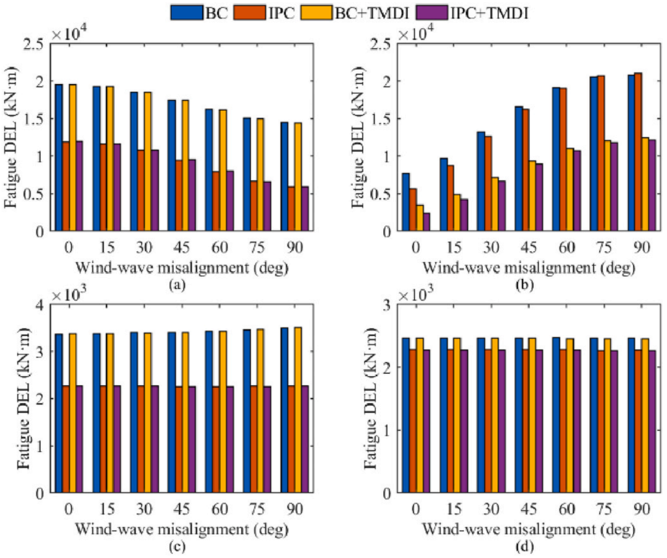

Fig. 11. DELs of FOWT under different wind-wave misalignment loads. (a) Tower base fore-aft bending moment. (b) Tower base side-to-side bending moment. (c) Blade root out-of-plane bending moment. (d) Blade root in-plane bending moment.

misalignment angle, and Fig. 11 compares fatigue DELs of tower and blade bending moments, obtained using four control strategies under a variety of wind-wave misalignment angles. The DELs are calculated using fixed amplitude loads at a frequency of 1 Hz. Furthermore, the first 100 s of the time-history response is excluded to prevent the initial conditions from influencing results.

Fig. 11(a) and (b) illustrate that the fatigue DEL of the tower base fore-aft bending moment increases with the wind-wave misalignment degree, whereas the side-to-side DEL exhibits an opposite trend. Especially, when the misalignment angle is higher than around 60°, under BC controller without TMDI, the side-to-side DEL exceeds the figure for the fore-aft direction. According to IEC 61400–6 (International Electrotechnical Commission, 2020), for tubular steel towers, the usage of the dominant (normally fore-aft direction) bending moment can be considered sufficient for the fatigue verification but under wind-wave misalignment conditions, tower side-to-side bending moments are too high to be ignored. This might be the reason why wind-wave misalignment must be considered in fatigue design load cases in IEC 61400–1 (International Electrotechnical Commission, 2019). This implies that mitigating the tower side-to-side response is equally crucial as reducing the tower fore-aft response under conditions of wind-wave misalignment.

Fig. 11 (a) and (b) also show that IPC can greatly mitigate tower fore-aft DEL under all wind-wave misalignment conditions. Apart from this, it slightly reduces tower side-to-side DEL under wind-wave alignment and small misalignment angles (0°–60°) but performs even worse than BC in strong misalignment conditions (75°, 90°). This suggests that IPC could be utilized to mitigate the fore-aft DEL but should not be considered to mitigate the side-to-side DEL, which is exactly the design target of IPC in this study. In contrast to IPC, it is observed that TMDI doesn't work in mitigating the tower fore-aft DEL but performs quite well in suppressing the side-to-side DEL. This is quite understandable because the TMDI is mounted in side-to-side direction. Hence, the cooperative control strategy combines the best of both IPC and TMDI, therefore mitigating fore-aft as well as side-to-side bending moment DELs.

Besides, it is visible from Fig. 11 (c) and (d) that the blade out-of-plane and in-plane DELs remain unchanged in a variety of wind-wave misalignment degrees. IPC can greatly alleviate out-of-plane DEL and slightly mitigate in-plane DEL, but TMDI doesn't work in both terms, so the cooperative control strategy inherits the strength of IPC and performs the same as that. Given that wind-wave misalignment and TMDI barely impact the blade DELs, the subsequent study focuses on the impact of the cooperative control method on the tower response under wind-wave misalignment.

Cycle loading-related fatigue damage frequently begins at the surface and gradually progresses to failure. It could happen even if the stresses are less than the material's yield strength. Given that the tower bending moments in both directions contribute to the axial stress as Eq. (30), stress-based fatigue damage assessment is essential for FOWT towers. Fig. 10 shows the bending moments acting on the tower, where the axial stresses of different positions on the tower cross-section can be calculated as follows:

$$\sigma_L = \frac{F_z}{A_{cr}} + \frac{M_x x_c}{I_x} + \frac{M_y y_c}{I_y} \tag{30}$$

Similar to the fatigue DEL, the fatigue damage-equivalent stresses (DESs) of different positions on the tower cross-section can be obtained as follows (Hayman, 2012):

$$DES^{ST} = \left(\frac{\sum_i (n_i \sigma_i)^m}{f_{eq} T_e}\right)^{1/m} \tag{31}$$

where σ_i is the stress range and other parameters are the same as those in Eq. (29).

Fig. 12 shows the DES distribution in the whole tower base cross-section, from which it is clearly visible that the cooperative control strategy can minimize the DES in almost the whole tower cross-section

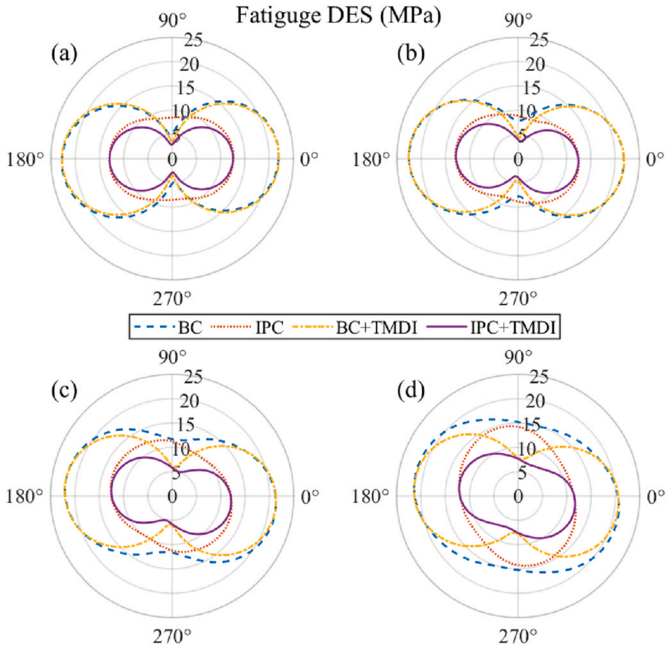

Fig. 12. Fatigue DES distribution of FOWT tower base subjected to various wind-wave misalignments. (a) Aligned. (b) 30° misalignment. (c) 60° misalignment. (d) 90° misalignment.

and all wind-wave misalignment conditions. The fatigue DESs in the critical position, where the DES is the maximum value among the entire cross-section, are further shown in Fig. 13. Similar to the trends of tower fore-aft and side-to-side DELs, the fatigue DES for IPC grows with the rise of wind-wave misalignment degree, while the figure for TMDI drops as the misalignment angle increases. The fatigue DES under the cooperative control strategy is always almost the same, staying at the minimum. Additionally, the critical position under all control strategies drifts when the wind-wave misalignment angle rises, which provides a reference for the maintenance of the FOWT tower.

Fig. 14 compares the mean power and error RMS of FOWT under four control strategies. There is no difference between various wind-wave loadings, which indicates the stability of controllers in power regulation under complex wind-wave misalignment conditions. The mean power under IPC is a little bit lower than that for BC, but the former's error RMS is much lower than the latter, showing better power regulation and higher power quality. TMDI has no influence on the power regulation of IPC, so the cooperative control strategy inherits those benefits from IPC.

4. Fatigue life estimation based on site-specific conditions

The fatigue analysis of the FOWT tower considers site-specific conditions, with the Xiangshan wind farm in China's East China Sea, as shown in Fig. 15 (a), located 25 km offshore, serving as a representative wind-wave misalignment case. Fig. 15. (b) and Table 2 display the load conditions for this offshore wind farm.

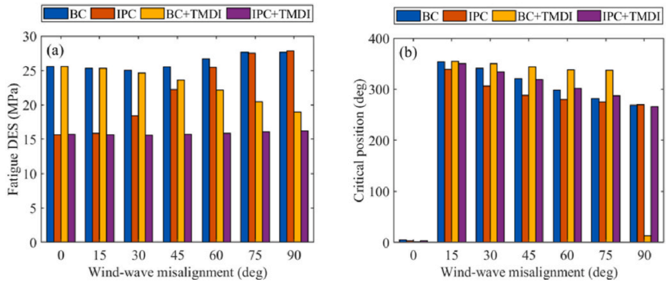

Fig. 13. DES in critical position (a) Value. (b) Critical Position.

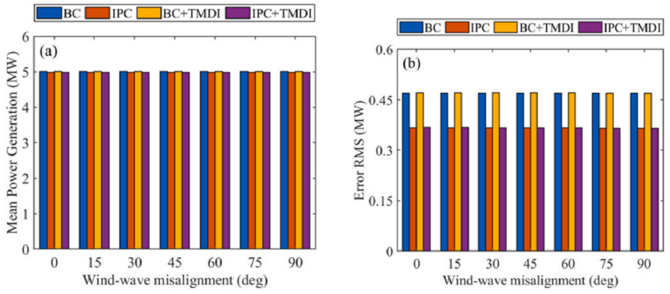

Fig. 14. (a) Mean power. (b) Power error RMS.

The fatigue life of the FOWT tower is predicted using the rainflow algorithm (Downing and Socie, 1982), and the double-slope S-N curve from DNV-OS-J101 (DNV-OS-J101, 2014) is used to predict the cycle number for the tower material based on the stress range that is determined from the time history response, as follows:

$$\log_{10} N = \log_{10} a - m \log_{10}\left(\Delta\sigma\left(\frac{t}{t_{ref}}\right)^{k}\right) \tag{32}$$

where N represents the cycle count; $\Delta\sigma$ represents the stress range; m is the negative inverse slope of S-N curve; $\log_{10} a$ is the intercept of mean S-N curve with the log N axis; t and t_{ref} are the component thickness and reference thickness, respectively, and if $t < t_{ref}$, $t/t_{ref} = 1$; k is the thickness exponent. Table 3 lists the values for these parameters.

The damage accumulation is evaluated using Miner's rule (Miner, 2021). The short-term damage rate from the jth time-history stress is calculated as follows:

$$DR_j^{ST} = \frac{D_j^{ST}}{T_j} \tag{33}$$

$$D_j^{ST} = \sum_i \frac{n_{ji}}{N_{ji}} \tag{34}$$

where T_j is the elapsed time of time-series j; n_{ji} is the cycle count; N_{ji} is the allowable cycle number. The lifetime short-term damage-rate can be predicted considering the load probability, as presented in Table 2. Therefore, the lifetime short-term damage-rate is:

$$D^{ST} = \sum_j f_j^L D_j^{ST} \tag{35}$$

and the predicted fatigue life is:

$$L_F = 1/D^{ST} \tag{36}$$

Figs. 16 and 17 show the shore-term damage rate of the FOWT tower. The cooperative control strategy can always realize a low damage rate in almost all cases. Although IPC can reduce the damage rate in wind-wave alignment and weak wind-wave misalignment conditions, it performs terribly in strong wind-wave misalignment situations since it cannot regulate tower side-to-side vibration which takes up a considerable percentage in fatigue stress contribution under strong wind-wave misalignment situations.

The final estimated fatigue life of the FOWT tower is shown in Fig. 18 and Table 4, from which the fatigue life under IPC is the same as that for the cooperative control strategy in wind-wave alignment and 15° wind-wave misalignment conditions, but it decreases with the rise of the wind-wave misalignment degree. In strong wind-wave misalignment conditions, IPC performs even worse than BC. With the assistance of TMDI, the cooperative control strategy enables high fatigue life for the FOWT tower in all wind-wave misalignment conditions. In strong wind-wave

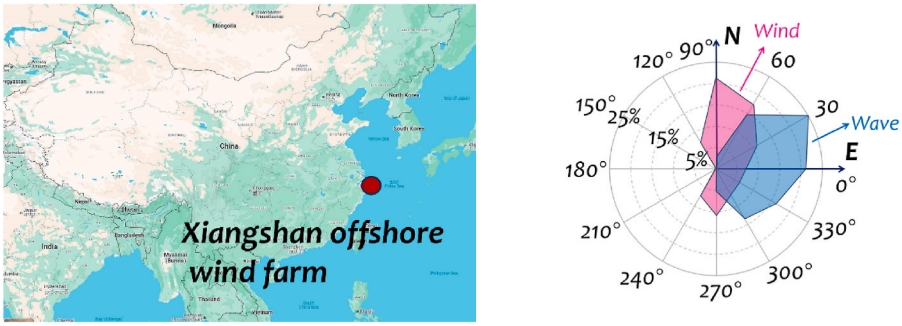

(a) Location of the Xiangshan wind farm (b) Probability distribution of load direction

Fig. 15. The location and load conditions of Xiangshan wind farm (Wang et al., 2024; Chen et al., 2024).

Table 2
Load cases in Xiangshan offshore wind farm [(Wang et al., 2024), (Chen et al., 2024)].

Load case	Wind speed V (m/s)	Significant wave height H_s (m)	Wave period T_p (m)	Occurrence probability P_f (%)
1	4	0.37	4.00	14.025
2	6	0.44	4.70	19.220
3	8	0.62	4.70	18.142
4	10	0.84	5.10	14.014
5	12	1.13	5.60	10.335
6	14	1.53	6.10	7.542
7	16	2.03	6.70	5.178
8	18	2.41	7.30	3.634
9	20	2.86	7.90	1.917
10	22	3.33	8.60	0.857
11	24	3.41	7.90	0.301

Table 3
S–N curves parameters.

$N < 10^7$ $\Delta\sigma > 52.63$	m_1	$N > 10^7$ $\Delta\sigma \leq 52.63$	m_2	k	t	t_{ref}
$\log_{10}a_1$		$\log_{10}a_2$				
12.164	3	15.606	5	0.2	0.027	0.032

misalignment conditions, the estimated fatigue life for the cooperative control strategy is several times those for other three control methods.

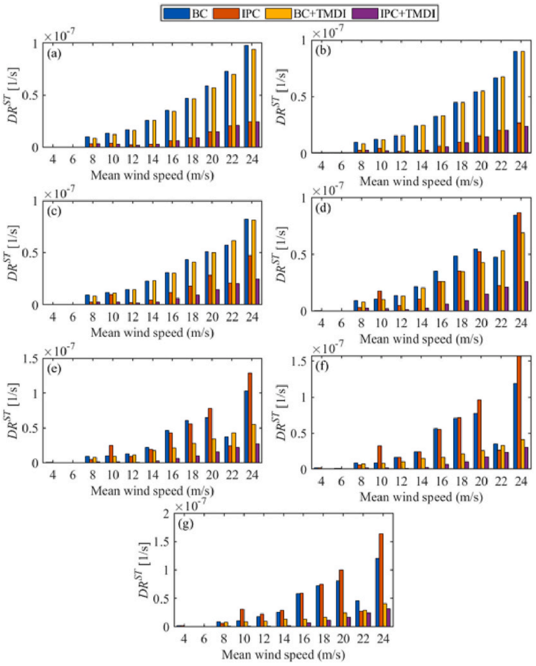

Fig. 16. Shore-term damage rate not considering the probability of load occurrence. (a) Aligned. (b) 15° misaligned. (c) 30° misaligned. (d) 45° misaligned. (e) 60° misaligned. (f) 75° misaligned. (g) 90° misaligned.

5. Conclusion and discussion

This study proposes a cooperative control strategy combining IPC with TMDI to mitigate FOWT tower fatigue under wind-wave misalignment. A 22-DOF nonlinear FOWT model is developed, incorporating IPC with an LQ-integral controller and a TMDI. The cooperative strategy is evaluated against three alternatives under steady wind, no-wave, and wind-wave misalignment conditions. Blade and tower DELs, tower DESs, mean power, and error RMS are analyzed for performance assessment. Finally, the tower's fatigue life is estimated using site-specific loading and damage accumulation theory. Key conclusions are presented.

(1) The side-to-side TMDI at the tower top only reduces the tower side-to-side response, having little impact on other responses. Besides, IPC can reduce the 1P oscillations of the blades, and it mitigates tower fore-aft response mostly by regulating the platform pitch motion. Hence, the cooperative control strategy not only can utilize IPC to reduce blade loads but also can further mitigate the tower structural response through the combination of the IPC and TMDI.

(2) With the rise of the wind-wave misalignment degree, the tower fore-aft bending moment fatigue DEL declines but the side-to-side DEL grows, and the blade DEL stays constant. Hence, it is essential to suppress the tower side-to-side response under wind-wave misaligned loads. Under these conditions, the cooperative control strategy proves to be more effective in mitigating the tower response compared to the individual application of either IPC or TMDI, minimizing the DES at almost all points in the tower section, including the critical position.

(3) Using the Xiangshan offshore wind farm's loading conditions, the cooperative control strategy reduces tower fatigue in most cases, particularly under strong wind-wave misalignment. The FOWT tower's fatigue life exceeds 10 years in all wind-wave misalignments and is at least four times longer than with the BC.

In civil engineering, inertial devices are usually implemented by ball screws and gear racks, which make the practical TMDI complex.

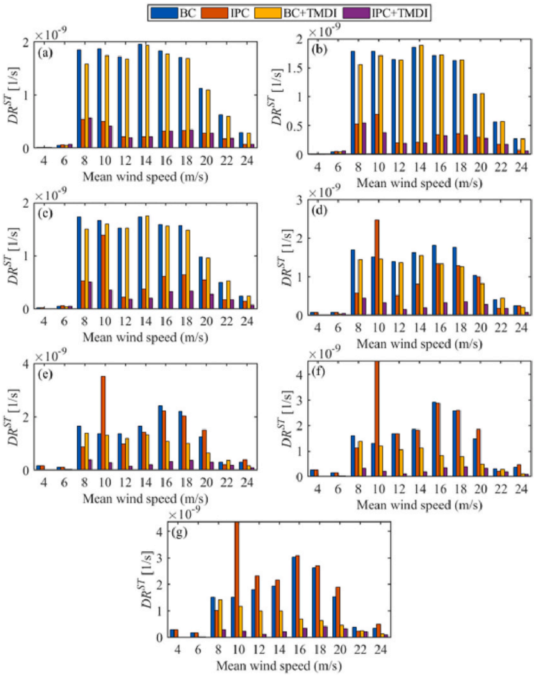

Fig. 17. Shore-term damage rate considering the probability of load occurrence. (a) Aligned. (b) 15° misaligned. (c) 30° misaligned. (d) 45° misaligned. (e) 60° misaligned. (f) 75° misaligned. (g) 90° misaligned.

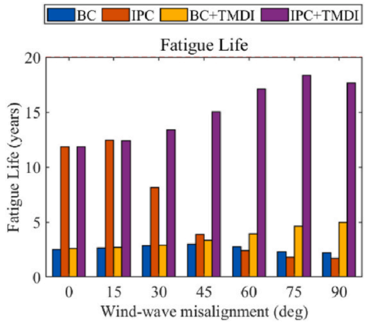

Fig. 18. Predicted fatigue life of FOWT tower.

Table 4
Expected fatigue life.

		0°	15°	30°	45°	60°	75°	90°
Fatigue life (years)	BC	2.5	2.6	2.8	3.0	2.7	2.3	2.2
	IPC	11.9	12.4	8.1	3.9	2.4	1.8	1.7
	BC + TMDI	2.6	2.7	2.9	3.3	3.9	4.7	5.0
	IPC + TMDI	11.9	12.4	13.4	15.0	17.1	18.34	17.6

Precision components in TMDI may need maintenance during long-term operation, which places higher requirements on reliability design. In addition, the nacelle space is limited and there is the need for the drivetrain, the generator, the control system and other equipment installation, which affects the TMDI stroke. These factors will make it hard for the TMDI to achieve the ideal control effect.

In addition, some assumptions are made in the dynamic simulation and controller design, such as the modal truncation assumption: flexible components such as towers and blades are modeled by finite mode expansion; small angle approximation: the coordinate transformation of each component uses a small angle linear approximation to calculate the rotation matrix; simplified aerodynamic modeling: the BEM method is used, combined with the wind field generated by TurbSim, which does not include dynamic stall or three-dimensional unsteady effects; simplified hydrodynamic model: the Morison's equation with Strip Theory is used to estimate the hydrodynamic force, considering only viscous resistance and added mass; simplified TMDI modeling: in the TMDI parameter optimization stage, a 2-degree-of-freedom equivalent simplified model is introduced. These assumptions are introduced to simply and quickly perform dynamic analysis and control performance evaluation, but they will affect the analysis accuracy to a certain extent. But overall, these assumptions are commonly used and will not completely overturn the analysis results.

CRediT authorship contribution statement

Yida Pu: Writing – original draft, Software, Resources, Methodology, Investigation, Formal analysis, Data curation, Conceptualization. **You Dong:** Writing – review & editing, Supervision, Resources, Project administration, Methodology, Investigation, Funding acquisition, Conceptualization. **Breiffni Fitzgerald:** Writing – review & editing, Supervision, Software, Resources, Methodology, Investigation, Conceptualization.

Funding

This work is supported by Research Grants Council (Research Impact Fund (RIF) project, R5006-23), HKSAR, China, Research Ireland grant no. 20/FFP-P/8702 and the Research Ireland project NexSys grant no. 21/SPP/3756.

Declaration of competing interest

The authors declare that they have no known competing financial interests or personal relationships that could have appeared to influence the work reported in this paper.

Appendix

Table. A1
DOFs considered in the FOWT model

q_{S_g}	Platform surge
q_{S_w}	Platform sway
q_{H_v}	Platform heave
q_R	Platform roll
q_P	Platform pitch
q_Y	Platform yaw
q_{TFA1}	First tower fore-aft bending mode
q_{TFA2}	Second tower fore-aft bending mode
q_{TSS1}	First tower side-to-side bending mode
q_{TSS2}	Second tower side-to-side bending mode
q_{yaw}	Nacelle yaw
q_{GeAz}	Generator azimuth angle
q_{DrTr}	Drive-train torsional flexibility
q_{B_iF1}	First flapwise bending mode for *i*th blade
q_{B_iF2}	Second flapwise bending mode for *i*th blade
q_{B_iE1}	First edgewise bending mode for *i*th blade
q_D	TMDI

References

Avendaño-Valencia, L.D., Abdallah, I., Chatzi, E., 2021. Virtual fatigue diagnostics of wake-affected wind turbine via gaussian process regression. Renew. Energy 170, 539–561. https://doi.org/10.1016/j.renene.2021.02.003.

Bir, G.S., 2010. User's Guide to MBC3: Multi-Blade Coordinate Transformation Code for 3-Bladed Wind Turbines. National Renewable Energy Laboratory. Technical Report NREL/TP-500-44327.

Bossanyi, E.A., 2003. Individual blade pitch control for load reduction. Wind Energy 6, 119–128. https://doi.org/10.1002/we.76.

Chen, Z.J., Stol, K.A., Mace, B.R., 2017. Wind turbine blade optimisation with individual pitch and trailing edge flap control. Renew. Energy 103, 750–765. https://doi.org/10.1016/j.renene.2016.11.009.

Chen, D., Huang, S., Huang, C., Liu, R., Ouyang, F., 2021. Passive control of jacket–type offshore wind turbine vibrations by single and multiple tuned mass dampers. Mar. Struct. 77, 102938. https://doi.org/10.1016/j.marstruc.2021.102938.

Chen, Z., Wang, L., Wang, L., Hong, Y., Zhang, B., Yang, Q., 2024. Integrated analysis of hybrid control for offshore wind turbines: a case study in wave resonance prone wind farms. Ocean. Eng. 298, 117176. https://doi.org/10.1016/j.oceaneng.2024.117176.

Dinh, V.-N., Basu, B., 2015. Passive control of floating offshore wind turbine nacelle and spar vibrations by multiple tuned mass dampers: PASSIVE CONTROL OF FLOATING WIND TURBINES BY MTMDs. Struct. Control Health Monit. 22, 152–176. https://doi.org/10.1002/stc.1666.

DNV-OS-J101, 2014. Design of Offshore Wind Turbine Structures.

Downing, S.D., Socie, D.F., 1982. Simple rainflow counting algorithms. Int. J. Fatigue 4, 31–40. https://doi.org/10.1016/0142-1123(82)90018-4.

Dueñas-Osorio, L., Basu, B., 2008. Unavailability of wind turbines due to wind-induced accelerations. Eng. Struct. 30, 885–893. https://doi.org/10.1016/j.engstruct.2007.05.015.

Fischer, T., Rainey, P., Bossanyi, E., Kühn, M., 2011. Study on control concepts suitable for mitigation of loads from misaligned wind and waves on offshore wind turbines supported on monopiles. Wind Eng. 35, 561–573. https://doi.org/10.1260/0309-524X.35.5.561.

Fitzgerald, B., Basu, B., 2020. Vibration control of wind turbines: recent advances and emerging trends. Int. J. Sustain. Mater. Struct. Syst. 4, 347. https://doi.org/10.1504/IJSMSS.2020.109090.

Fitzgerald, B., Sarkar, S., 2024. Observer based pitch control for load mitigation and power regulation of floating offshore wind turbines. J. Phys. Conf. Ser. 2647, 032003. https://doi.org/10.1088/1742-6596/2647/3/032003.

Fitzgerald, B., Basu, B., Nielsen, S.R.K., 2013. Active tuned mass dampers for control of in-plane vibrations of wind turbine blades: active tuned mass dampers. Struct. Control Health Monit. 20, 1377–1396. https://doi.org/10.1002/stc.1524.

Fitzgerald, B., McAuliffe, J., Baisthakur, S., Sarkar, S., 2023. Enhancing the reliability of floating offshore wind turbine towers subjected to misaligned wind-wave loading using tuned mass damper inerters (TMDIs). Renew. Energy 211, 522–538. https://doi.org/10.1016/j.renene.2023.04.097.

G.W.E. Council, 2024a. Global Wind Report 2024, Glob. Wind Energy Counc. Bonn Ger.

G.W.E. Council, 2024b. Global Offshore Wind Report 2024, GWEC Bruss. Belg.

Hall, M., 2015. MoorDyn user's guide. Dep. Mech. Eng. Univ. Maine Orono ME USA 15.

Hayman, G., 2012. Mlife Theory Manual for Version 1.00, Natl. Renew. Energy Lab. Gold, vol. 74. CO, p. 106.

International Electrotechnical Commission, 2019. Wind Energy Generation Systems – Part 1: Design Requirements, IEC6vols. 1400–1.

International Electrotechnical Commission, 2020. Wind Energy Generation Systems – Part 6: Tower and Foundation Design Requirements. IEC61400-6.

Jahangiri, V., Sun, C., 2020. Three-dimensional vibration control of offshore floating wind turbines using multiple tuned mass dampers. Ocean. Eng. 206, 107196. https://doi.org/10.1016/j.oceaneng.2020.107196.

Jonkman, B.J., 2009. Turbsim user's guide, Version 1.50. https://doi.org/10.2172/965520.

Jonkman, J., 2010. Definition of the floating system for phase IV of OC3. https://doi.org/10.2172/979456.

Jonkman, J.M., Buhl, M.L.Jr., 2005. FAST User's guide - updated August 2005. https://doi.org/10.2172/15020796.

Jonkman, J., Matha, D., 2009. *Quantitative Comparison of the Responses of Three Floating Platforms*.

Jonkman, J., Butterfield, S., Musial, W., Scott, G., 2009. Definition of a 5-MW reference wind turbine for offshore system development. https://doi.org/10.2172/947422.

Kane, T.R., Levinson, D.A., 1985. Dynamics, Theory and Applications. McGraw Hill.

KhalafAnsar, H.M., Keighobadi, J., 2023. Adaptive inverse deep reinforcement lyapunov learning control for a floating wind turbine. Sci. Iran. https://doi.org/10.24200/sci.2023.61871.7532.

Lemmer, F., Schlipf, D., Cheng, P.W., 2016. Control design methods for floating wind turbines for optimal disturbance rejection. J. Phys. Conf. Ser. 753, 092006. https://doi.org/10.1088/1742-6596/753/9/092006.

Li, T., Liu, Z., Liu, S., Fan, Y., Yang, Q., Xiao, H., 2022. Numerical study on passive structural control of semi-submersible floating wind turbine considering non-collinear wind and waves. Ocean. Eng. 266, 112745. https://doi.org/10.1016/j.oceaneng.2022.112745.

Lin, J., Wang, Y., Zhang, G., Liu, Y., Zhang, J., 2024. Novel tuned mass dampers installed inside tower of spar offshore floating wind turbines. Ocean. Eng. 301, 117412. https://doi.org/10.1016/j.oceaneng.2024.117412.

Marian, L., Giaralis, A., 2014. Optimal design of a novel tuned mass-damper–inerter (TMDI) passive vibration control configuration for stochastically support-excited structural systems. Probabilistic Eng. Mech. 38, 156–164. https://doi.org/10.1016/j.probengmech.2014.03.007.

MathWorks Inc, 2023. MATLAB Version: 9.14. (R2023A).

Miner, M.A., 2021. Cumulative damage in fatigue. J. Appl. Mech. 12, A159–A164. https://doi.org/10.1115/1.4009458.

Namik, H., Stol, K., 2010. Individual blade pitch control of floating offshore wind turbines. Wind Energy 13, 74–85. https://doi.org/10.1002/we.332.

Namik, H., Stol, K., 2014. Individual blade pitch control of a spar-buoy floating wind turbine. IEEE Trans. Control Syst. Technol. 22, 214–223. https://doi.org/10.1109/TCST.2013.2251636.

Novaes Menezes, E.J., Araújo, A.M., Rohatgi, J.S., González Del Foyo, P.M., 2018. Active load control of large wind turbines using state-space methods and disturbance accommodating control. Energy 150, 310–319. https://doi.org/10.1016/j.energy.2018.02.143.

Odgaard, P.F., Larsen, L.F.S., Wisniewski, R., Hovgaard, T.G., 2016. On using pareto optimality to tune a linear model predictive controller for wind turbines. Renew. Energy 87, 884–891. https://doi.org/10.1016/j.renene.2015.09.067.

Park, S., Lackner, M.A., 2021. Edgewise vibration suppression of multi-megawatt wind turbine blades using passive tuned mass dampers. Wind Eng. 45, 1082–1100. https://doi.org/10.1177/0309524X20953810.

Pierson Jr., W.J., Moskowitz, L., 1964. A proposed spectral form for fully developed wind seas based on the similarity theory of SA kitaigorodskii. J. Geophys. Res. 69, 5181–5190.

Sarkar, S., Fitzgerald, B., 2020. Vibration control of spar-type floating offshore wind turbine towers using a tuned mass-damper-inerter. Struct. Control Health Monit. 27, e2471. https://doi.org/10.1002/stc.2471.

Sarkar, S., Fitzgerald, B., 2021. Use of kane's method for multi-body dynamic modelling and control of spar-type floating offshore wind turbines. Energies 14, 6635. https://doi.org/10.3390/en14206635.

Sarkar, S., Fitzgerald, B., 2022. Fluid inerter for optimal vibration control of floating offshore wind turbine towers. Eng. Struct. 266, 114558. https://doi.org/10.1016/j.engstruct.2022.114558.

Sarkar, S., Fitzgerald, B., Basu, B., 2020a. Nonlinear model predictive control to reduce pitch actuation of floating offshore wind turbines. IFAC-Pap. 53, 12783–12788. https://doi.org/10.1016/j.ifacol.2020.12.1936.

Sarkar, S., Chen, L., Fitzgerald, B., Basu, B., 2020b. Multi-resolution wavelet pitch controller for spar-type floating offshore wind turbines including wave-current interactions. J. Sound Vib. 470, 115170. https://doi.org/10.1016/j.jsv.2020.115170.

Sarkar, S., Fitzgerald, B., Basu, B., 2021. Individual blade pitch control of floating offshore wind turbines for load mitigation and power regulation. IEEE Trans. Control Syst. Technol. 29, 305–315. https://doi.org/10.1109/TCST.2020.2975148.

Si, Y., Karimi, H.R., Gao, H., 2014. Modelling and optimization of a passive structural control design for a spar-type floating wind turbine. Eng. Struct. 69, 168–182. https://doi.org/10.1016/j.engstruct.2014.03.011.

Smith, M.C., 2002. Synthesis of mechanical networks: the inerter. IEEE Trans. Autom. Control 47, 1648–1662. https://doi.org/10.1109/TAC.2002.803532.

Sun, C., 2018. Semi-active control of monopile offshore wind turbines under multi-hazards. Mech. Syst. Signal Process. 99, 285–305. https://doi.org/10.1016/j.ymssp.2017.06.016.

Tang, J., Dai, K., Luo, Y., Bezabeh, M.A., Ding, Z., 2024. Integrated control strategy for the vibration mitigation of wind turbines based on pitch angle control and TMDI systems. Eng. Struct. 303, 117529. https://doi.org/10.1016/j.engstruct.2024.117529.

Wakui, T., Nagamura, A., Yokoyama, R., 2021. Stabilization of power output and platform motion of a floating offshore wind turbine-generator system using model predictive control based on previewed disturbances. Renew. Energy 173, 105–127. https://doi.org/10.1016/j.renene.2021.03.112.

Wang, L., Wang, L., Hong, Y., 2024. Mitigation of side-to-side vibration of a 10MW monopile offshore wind turbine under misaligned wind and wave conditions by an active torque control. J. Sound Vib. 574, 118225. https://doi.org/10.1016/j.jsv.2023.118225.

Wright, A.D., 2004. Modern control design for flexible wind turbines. https://doi.org/10.2172/15011696.

Wu, Z., Li, Y., 2020. Platform stabilization of floating offshore wind turbines by artificial muscle based active mooring line force control. IEEE ASME Trans. Mechatron. 25, 2765–2776. https://doi.org/10.1109/TMECH.2020.2992711.

Xie, J., Dong, H., Zhao, X., 2024. Power regulation and load mitigation of floating wind turbines via reinforcement learning. IEEE Trans. Autom. Sci. Eng. 1–12. https://doi.org/10.1109/TASE.2023.3295576.

Yuan, Y., Tang, J., 2017. Adaptive pitch control of wind turbine for load mitigation under structural uncertainties. Renew. Energy 105, 483–494. https://doi.org/10.1016/j.renene.2016.12.068.

Yuan, Y., Chen, X., Tang, J., 2020. Multivariable robust blade pitch control design to reject periodic loads on wind turbines. Renew. Energy 146, 329–341. https://doi.org/10.1016/j.renene.2019.06.136.

Zhang, C., Plestan, F., 2021a. Individual/Collective blade pitch control of floating wind turbine based on adaptive second order sliding mode. Ocean. Eng. 228, 108897. https://doi.org/10.1016/j.oceaneng.2021.108897.

Zhang, C., Plestan, F., 2021b. Adaptive sliding mode control of floating offshore wind turbine equipped by permanent magnet synchronous generator. Wind Energy 24, 754–769. https://doi.org/10.1002/we.2601.

Zhang, Z., Nielsen, S., Blaabjerg, F., Zhou, D., 2014. Dynamics and control of lateral tower vibrations in offshore wind turbines by means of active generator torque. Energies 7, 7746–7772. https://doi.org/10.3390/en7117746.

Zhang, Y., Yang, X., Liu, S., 2022. Data-driven predictive control for floating offshore wind turbines based on deep learning and multi-objective optimization. Ocean. Eng. 266, 112820. https://doi.org/10.1016/j.oceaneng.2022.112820.

Zuo, H., Bi, K., Hao, H., 2017. Using multiple tuned mass dampers to control offshore wind turbine vibrations under multiple hazards. Eng. Struct. 141, 303–315. https://doi.org/10.1016/j.engstruct.2017.03.006.